Strain and Defect Engineering on Phase Transition of Monolayer Black Phosphorene

Journal:	*Physical Chemistry Chemical Physics*
Manuscript ID	CP-ART-02-2018-001334.R1
Article Type:	Paper
Date Submitted by the Author:	19-May-2018

Complete List of Authors:	Chen, Yan; Xi'an Jiaotong University, School of Aerospace Shi, Xiaoyang; Columbia University Li, Mingjia; Xi'an Jiaotong University Liu, Yilun; Xi'an Jiaotong University, School of Aerospace Xiao, Hang; Columbia University, Chen, Xi; Columbia University

Strain and Defect Engineering on Phase Transition of Monolayer Black Phosphorene

Yan Chen[1], Xiaoyang Shi[2], Mingjia Li[3], Yilun Liu[4,*], Hang Xiao[2,5,*] and Xi Chen[2,5]

[1] International Center for Applied Mechanics, State Key Laboratory for Strength and Vibration of Mechanical Structures, School of Aerospace, Xi'an Jiaotong University, Xi'an 710049, China

[2] Columbia Nanomechanics Research Center, Department of Earth and Environmental Engineering, Columbia University, New York, NY 10027, USA

[3] Key Laboratory of Thermo-Fluid Science and Engineering of MOE, School of Energy and Power Engineering, Xi'an Jiaotong University, Xi'an 710049, China

[4] State Key Laboratory for Strength and Vibration of Mechanical Structures, School of Aerospace, Xi'an Jiaotong University, Xi'an 710049, China

[5] School of Chemical Engineering, Northwest University, Xi'an 710069, China

[*] E-mail: (Y.L.) yilunliu@mail.xjtu.edu.cn; (H.X.) hx2152@columbia.edu

Abstract: The phase transition of monolayer black phosphorene (MBP, α-P) to β-P and γ-P are explored by density functional theory (DFT) calculations and molecular dynamics (MD) simulations using reactive force field. It is found that MBP can transfer to a mixed phase of β-P and γ-P under biaxial strain, while the Stone–Wales defect (SW-2) in MBP can serve as an excellent 'phase transition catalyzer', significantly decreasing the critical strain for phase transition and increasing the homogeneity of phase transition. The biaxial strain state (i.e. the strain components in armchair and zigzag direction) and loading mode (i.e. the proportional and staged loading) have significant effects on the phase transition of MBP. In general, the phase transition of MBP is driven by the tension strain in armchair direction, but the large tension or compression strain in zigzag direction can also promote the phase transition. Besides, the MBP has larger fracture strain under staged loading, generating more uniform phase transition structure. The effects of curvature and SW-2 defect concentration on phase transition of MBP are also studied, which shows easier phase transition for larger curvature and higher SW-2 defect concentration. The systematic results presented herein shed useful insights for designing and tuning the structure of MBP through phase transition facilitated by strain and defect engineering.

1. Introduction

After successfully exfoliated from its black phosphorus counterpart,[1-3] a novel two-dimensional (2-D) material, i.e. black phosphorene, has attracted a lot of research interests, thanks to its unique properties that are different from other 2-D materials, such as graphene, hexagonal boron nitride, silicene, transition metal dichalcogenide, etc.[4-10] Monolayer black phosphorene (MBP) has an inherent, direct and appreciable band gap which can be further tuned by simply controlling the layer number,[11] strain and orientation.[12] Besides, MBP has a high on/off ratio up to 10^4 at room temperature,[13] and its charge-carrier mobility could be up to 1,000 $cm^2V^{-1}s^{-1}$,[2] rendering it an promising material for semiconductor industry.

Recently, different types of monolayer phosphorus allotropes have been discovered in experiments [14, 15] and density functional theory (DFT) calculations.[16-18] Based on *ab initio* DFT calculations, Zhu et al.[17] investigated a new layered structure of phosphorus called blue phosphorus (β-P), whose monolayer structure displays a wide intrinsic band gap of about 2 eV. Furthermore, a potential transformation pathway from MBP to blue phosphorene with an energy barrier of about 0.47 eV/atom has been proposed as a possible way to synthesize β-P. Guan et al. found other two stable layered phosphorus allotropes (γ-P and δ-P), and the energy cost of connecting the different phases of phosphorus allotrope is negligible.[18] Based on these work, Wu et al.[16] further predicted nine new monolayer phosphorus allotropes composed of four phosphorus square or five phosphorus pentagon units, enormously distinguished from the previous honeycomb structures. Various monolayer phosphorus allotropes present disparate structures and result in abundant physical, chemical, thermal and mechanical properties,[17-23] rendering them promising 2-D materials in many nano-devices. Thus, phase transition among these monolayer phosphorus allotropes can regulate the structures and tune the corresponding functionalities and properties, enormously extending their applications.

Many efforts have been done to achieve the phase transition of 2-D materials, such as electrostatic gating, chemical doping, strain engineering, alloying,[24-29] aiming at a feature-rich material design. Li et al.[27] systematically studied phase transition in some monolayer transition metal dichalcogenides (TMDs) including monolayer $MoTe_2$ and MoS_2 by

electrostatic gating, which is readily available in experiments. Just recently, the electrostatic-doping-driven phase transition between different hexagonal phases (2H) and monoclinic phases (1T′) of monolayer molybdenum ditelluride ($MoTe_2$) has been realized in experiments.[30] Zhou et al.[26] found a phase switching between semiconducting H-$MoTe_2$ and semi-metallic T′-$MoTe_2$ by chemical doping of some common atoms and molecules. Duerloo et al.[25] demonstrated the phase diagrams of $Mo_{1-x}W_xTe_2$ alloy consisted of pure $MoTe_2$ and WTe_2, and the H-T′ phase transition temperature in $Mo_{1-x}W_xTe_2$ monolayer can be tuned by adjusting the alloy stoichiometry through W content. Kan et al. investigated a possible pathways of the phase transition of monolayer MoS_2 (H-MoS_2 → O-MoS_2→ DT-MoS_2→ ZT-MoS_2 → H-MoS_2) by inserting or extracting Lithium atoms from MoS_2 system.[31] Deng et al. predicted that a reversible phase transition between two stable Li doped black phosphorene phases (P_4Li_2) can be tuned by applying an external electric field with a maximum strain output of 2.06% for high frequency actuation applications.[28]

Strain engineering is regarded as an effective approach to tune the electronic structure,[32] chemical adsorption,[33] electrical conductance,[20] thermal conductivity,[34, 35] piezoelectricity effect[36] and piezophototronic effect[37] of many 2-D nanomaterials. Besides, strain engineering can also serve as a useful tool to regulate the phase transition of 2-D materials. Based on density functional and hybrid Hartree-Fock/density functional calculations, Duerloo et al.[29] predicted that $MoTe_2$ can be an excellent candidate of phase change materials among many 2-D monolayer Mo- and W- dichalcogenide compounds under biaxial substrate-induced strain. Even so, few works have been done to figure out the phase transition of 2-D nanomaterials through strain engineering, though it can be an effective tool experimentally.

Though MBP have many monolayer phosphorus allotropes, no phase transition among those 2-D nanomaterials has been directly observed in simulations or experiments, even though the pressure-induced phase transition between bulk black phosphorus (i.e. A17) and bulk blue phosphorus (i.e. A7) has been found before.[38, 39] Recently, we have observed a phase transition from MBP to a mixture of β-phase (β-P) and γ-phase (γ-P) for the Stone–Wales defective (SW-2) MBP under armchair tension.[40] However, many factors have not been considered, such as the biaxial strain state, loading mode, curvature, SW-2 defect concentration, etc. In this work we focus on the phase transition of SW-2 defective MBP,

which may be easily formed in MBP due to its low formation energy.[41] A comprehensive theoretical study has been done to investigate those factors that may affect the phase transition of MBP by combining *ab initio* DFT calculations and molecular dynamics (MD) simulations using a reactive force field (ReaxFF).

2. Models and methods

First, a 5 × 4 × 1 supercell (containing 80 Phosphorus atoms) of α-P and β-P with or without SW-2 defect was adopted to calculate the energy surface of α-P and β-P under different biaxial strain (to analysis the phase transition from α-P to β-P), as shown in figure 1(a) and (b). All *ab initio* DFT calculations were performed using QUANTUM ESPRESSO.[42] Electron exchange and correlation effects were described by the generalized gradient approximation (GGA) with Perdew, Burke, and Ernzerhof (PBE) parametrization.[43] Ultrasoft pseudopotentials were used to describe electron-ion interactions, a plane-wave cutoff energy of 30 Ry was used, and brillouin zone for the supercells was sampled by a 3 × 3 × 1 Monkhorst-Pack *k*-point mesh.[44] The system convergence was tested for cutoff energy and *k*-point mesh. All the structures were first relaxed without any symmetry constraint using conjugate gradient method (CG) until the energy and Helmann-Feynman force were converged within 10^{-6} eV and 10^{-2} eVÅ^{-1}, respectively. A vacuum layer of 2 nm was introduced in the perpendicular direction of the basal plane to minimize the interlayer interactions due to the periodic boundary condition. The relaxed lattice constants along the armchair and zigzag and directions are 4.625 Å and 3.298 Å for unit cell of MBP, and 5.676 Å and 3.277 Å for unit cell of monolayer β-P, in consistent with previous results.[17, 45, 46] Then, different biaxial strains in armchair and zigzag directions were applied to calculate the energy surface of α-P and β-P under biaxial strain state.

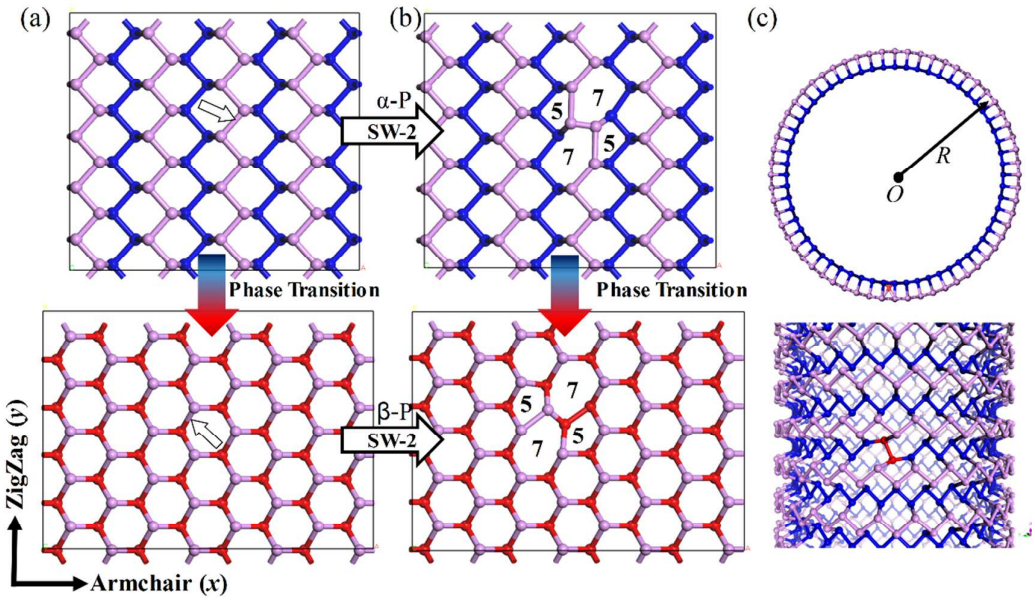

Figure 1. Atomic structures of pristine (a) and SW-2 defective (b) α-P and β-P for DFT calculations. (c) α-P nanotube with SW-2 defect.

The MD simulations were performed by using a Large-scale Atomic/Molecular Massively Parallel Simulator (LAMMPS)[47] and the interatomic interactions of P atoms were described by a reactive force field of P/H systems developed by Xiao et al.,[48] which can give good predictions of the physical and mechanical properties of MBP with SW defects and other phases of monolayer phosphorene (e.g. β-P and γ-P). The in-plane dimensions of MBP sheet were about 10 nm × 10 nm, and periodic boundary conditions were applied in three directions and a vacuum layer of 3 nm was introduced in *z* direction to eliminate the interaction of adjacent layers. Whereas for α-P nanotube (α-PNT, see figure 1(c)), the periodic boundary condition was applied in the tube axis direction and a vacuum layer of 6 nm was introduced in lateral directions to eliminate the interaction of adjacent α-PNTs. The thickness of MBP and α-PNT was set as 5.24 Å to calculate the in-plane stress in consistent with previous literatures.[49] The strain rate was set as 5×10^{-8} fs^{-1} without additional mentions. After equilibrium, uniaxial or biaxial strain was applied to the pristine and defective MBP or α-PNT by changing the dimensions of the simulation box in the loading directions step by step. The time step was set to 1 fs throughout the MD simulations, and the smaller time step of 0.5 fs is also tested, giving the same results. During uniaxial tension, the in-plane stress perpendicular

to the loading direction was kept at zero, and the system temperature was 400 K (to speed the phase transition) through Nose-Hoover barostat and thermostat, respectively. Here, the fracture strain was defined as the strain where the stress drops to zero. The tensile strength was defined as the maximum stress during tension and Young's modulus was defined as the slope of the stress-strain curve under tensile strain below 10%.

3. Results and discussions

3.1 Phase energetics under biaxial strain

In this section, we calculate the potential energy (defined as U) of α-P and β-P based on DFT calculations as a driven force[29] to explain the possibility of phase transition from α-P to β-P. Though the α-P (MBP) transforms to a mixed phase of β-P and γ-P under armchair tension according to our previous work,[40] the region adjacent to the SW-2 defect is dominated by β-P for all of the cases of phase transition at different temperatures and strain rates. Thus, we calculate the potential energy of pristine and SW-2 defective α-P and β-P under different biaxial strains with a 5 × 4 × 1 supercell based on DFT calculations, respectively. The equilibrium lattice constants (a × b) for SW-2 defective α-P and β-P is 18.81Å × 16.36 Å (defined as a_0 and b_0 below) and 22.78 A × 16.31 Å, respectively. The SW-2 defect has a small influence on the lattice constant. It is shown that the lattice difference between the SW-2 defective α-P and β-P is about 21.11% (for pristine α-P and β-P the difference is 22.72%) in the armchair direction, while it is almost the same in the zigzag direction. Thus, we can expect that the armchair tensile strain is necessary for phase transition from α-P to β-P.

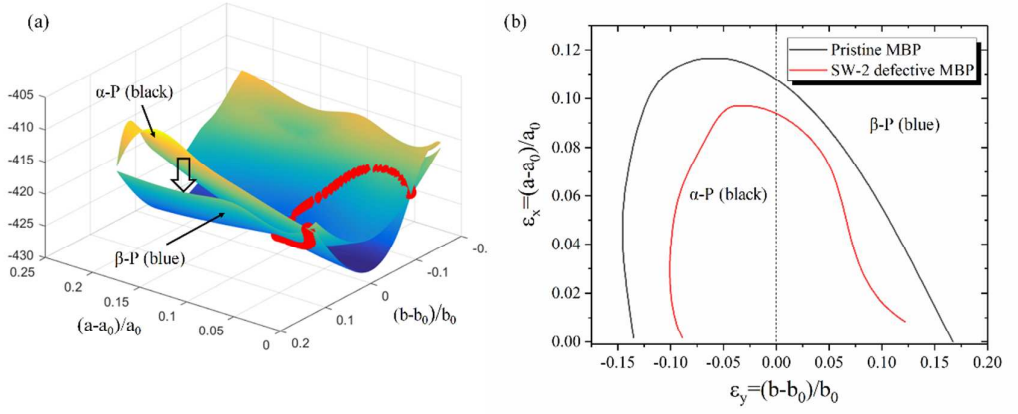

Figure 2. Phase energetics results based on DFT calculations. (a) Potential energy surface of monolayer α-P to β-P with a SW-2 defect under biaxial strain. The red points show the intersection of the potential energy surfaces between α-P and β-P. (b) The Intersection contour of energy surfaces of α-P and β-P with or without SW-2 defect. The strain is defined with respect to the equilibrium lattice constants of pristine and SW-2 defective α-P, respectively, where *a* is along the armchair direction *b* is along the zigzag direction.

We construct a 6 × 12 grids in (*a, b*) space to calculate the potential energy $U(a, b)$ of monolayer α-P and β-P with or without SW-2 defect under biaxial strain, respectively. As a result, a total of 72 points of $U(a, b)$ is obtained. Using the Lagrange interpolation method, we get the potential energy surface $U(a, b)$ of pristine and SW-2 defective monolayer α-P and β-P under biaxial strain, and the intersection of the two energy surfaces of SW-2 defective monolayer α-P and β-P is highlighted by red points in figure 2(a), which indicates the phase transition can occur in the view of potential energy. Here, the biaxial strain in α-P and β-P is defined with respect to the equilibrium lattice constants of α-P (i.e. a_0 and b_0). The potential energy surfaces of pristine monolayer α-P and β-P are similar to that of SW-2 defective monolayer α-P and β-P, thus not shown here.

Figure 2(b) gives the intersection contour of the energy surfaces with respect to strain in armchair and zigzag direction, which can be treated as the phase boundary between α-P and β-P with or without SW-2 defect at zero temperature, respectively. As the bending stiffness of 2-D materials is very small and they are easy to buckle under compression, we only consider the small compressive strain in zigzag direction (i.e. smaller than 0.15). Besides, the curved surface of MBP may also have a significant effect on the phase transition, which will be discussed from MD simulations with a larger supercell to figure out the buckling behaviors better.

Based on the phase boundary in figure 2(b), it is qualitatively shown that the phase transition of MBP is primarily driven by armchair tensile strain, and the phase transition is also promoted by the zigzag tensile strain. Besides, the small zigzag compressive strain prevents the phase transition, while the large zigzag compressive strain can significantly promote the phase transition so that the critical tensile strain in armchair direction for the

phase transition is significantly decreased with the increasing of compressive strain in zigzag direction, as shown in Figure 2(b). Besides, SW-2 defect can move inward the phase boundary remarkably, in the other word, SW-2 defect can promote the phase transition of α-P to β-P, serving as an effective "phase transition catalyzer". Considering the periodic boundary condition of box in DFT calculations, the distribution of SW-2 defect is uniformly distributed with density of 1 per 20 lattice units of MBP.

Note that the results presented herein only account for the ground state energy of the systems at 0 K without considering the zero-point vibrational energy or Helmholtz free energy at finite temperature.[40] In fact, the vibrational energy is only a small component of the free energy, whose influence is small according to the previous results of $MoTe_2$.[29] So, the overall trend of the intersection contour of energy surfaces changes little by considering the vibrational energy. Therefore, in this work we only use the ground state potential energy of α-P and β-P under biaxial strain as an energy criterion to give some useful outlines of the phase transition, and the results presented herein will give some qualitative but important references for studying the phase transition of MBP under finite temperature using MD simulations. As both of the two systems contain 80 atoms with total degree of freedoms (DOFs) 240, the DFT calculations of the dynamic process of phase transition is out of our computing ability. In the following Section, we use MD simulations with a reactive force field to study the dynamic phase transition process of pristine and SW-2 defective MBP by considering the effects of biaxial strain state, loading mode, curvature and SW-2 defect concentration.

3.2 Phase transition under biaxial proportional loading

According to the intersection contour of energy surfaces between α-P and β-P under biaxial strain, phase transition of MBP can be effectively tuned by the strain in armchair and zigzag direction. In this section, MD simulations are conducted to investigate the dynamic phase transition process of MBP under biaxial strain, as DFT calculations may be too expensive to investigate the dynamic process of a system with a large number of atoms. Here, the loading mode is the biaxial proportional loading, which means the strains in armchair and zigzag direction proportionally increase with time to the final values, as indicated in Figure 3(a).

For the proportional loading mode, different biaxial strain states are achieved by applying different loading rates in armchair and zigzag direction, which may be realized by proportionally controlling substrate-induced strain or through pressure-induced blister on circular or elliptic membrane, just as many previous works done on graphene or MoS_2.[50-53] Here, the strain rate in armchair direction for all of the cases is set as 5×10^{-8} fs^{-1}, and the strain rate in zigzag direction is set as different values to realize different biaxial strain state, as shown in Figure 3(a) and 3(b). In order to study the dynamic phase transition from MBP to the mixed phase of β-P and γ-P, the biaxial strain is applied to MBP and its atomic structure is tracked during MD simulations to determine the critical strain of phase transition. Both of the pristine and SW-2 defective MBP are simulated. Indeed, the phase transition of MBP is also influenced by strain rate which will be systematically studied in our future works.

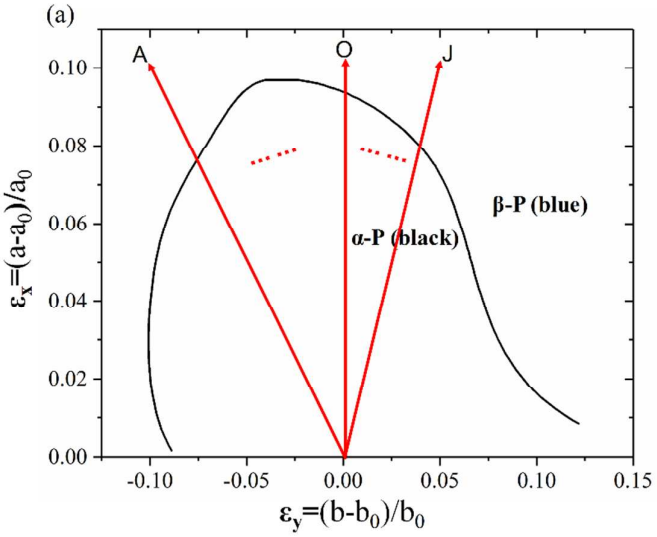

(b)

Tension	Strain rate (fs^{-1})	
	Armchair	Zigzag
A	5×10^{-8}	-5.0×10^{-8}
B	5×10^{-8}	-2.5×10^{-8}
C	5×10^{-8}	-1.0×10^{-8}
D	5×10^{-8}	-5.0×10^{-9}
E	5×10^{-8}	-1.0×10^{-9}
O	5×10^{-8}	0
F	5×10^{-8}	5.0×10^{-10}
G	5×10^{-8}	1.0×10^{-9}
H	5×10^{-8}	5.0×10^{-9}
I	5×10^{-8}	1.0×10^{-8}
J	5×10^{-8}	2.5×10^{-8}

Figure 3. The illustrations of the biaxial proportional loading. (a) The intersection contour of the two energy surfaces of SW-2 defective monolayer α-P and β-P under biaxial strain. The red lines indicate different loading paths. (b) Different strain rates in armchair and zigzag direction corresponding to different loading paths in (a). The settings for pristine monolayer α-P and β-P is just the same.

Figure 4 illustrates the critical strain in armchair direction for the phase transition of pristine and SW-2 defective MBP at different loading paths. Indeed, phase transition is observed for all of the MD simulation cases. For SW-2 defective MBP, as the loading path

changes from J to O, the critical strain of phase transition in armchair direction first increases, and gets a peak value of 0.2401 in armchair direction at loading path F, and then drops to 0.2117 for zero deformation in zigzag direction. While, for the compressive strain in zigzag direction, the critical strain in armchair direction first rises to the maximum value of 0.2529, and then decreases to 0.1824 for the loading path from O to A. For the pristine MBP, the similar trend of the critical strain for phase transition is observed, except that the value of the critical strain is larger than that of the SW-2 defective MBP, indicating that the SW-2 defect in MBP can effectively promote the phase transition. Note that the critical strain for phase transition presented herein corresponds to the beginning point of phase transition and the initial phase transition is from MBP to β-P in consistent with the phase boundaries obtained in Section 3.1. After the initiation of phase transition, the phase transition region quickly spreads and different phase transition modes (i.e. complete phase transition and local phase transition) are observed.

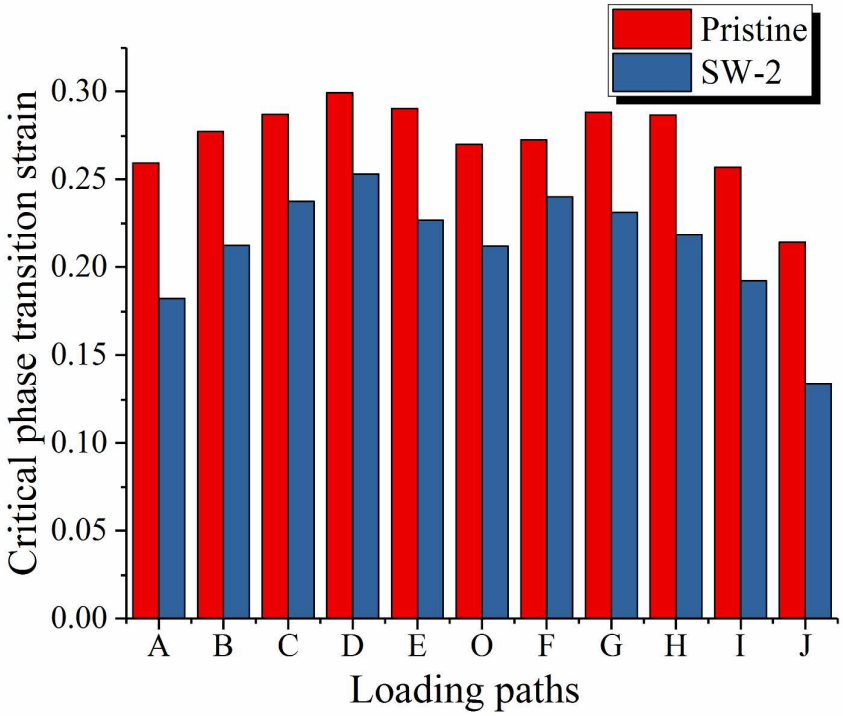

Figure 4. Critical strain in armchair direction for phase transition of SW-2 defective and pristine MBP under different loading paths. Different loading paths is obtained by changing the strain rate in zigzag direction corresponding to Figure 3.

For the biaxial proportional loading mode, the critical phase transition strain obtained from MD simulations has a similar trend to that of the intersection contour of the potential energy surfaces of SW-2 defective monolayer MBP and β-P obtained from DFT calculations. For example, the maximum critical strain in armchair direction for phase transition is obtained for small compressive strain in zigzag direction (i.e. -0.0253 for MD simulations and -0.048 for DFT calculations), indicating a small compressive strain in zigzag direction can prevent the phase transition. While, the large tensile or compressive strain in zigzag direction can promote the phase transition. Though the exact values of the critical strain for phase transition may not agree with each other, the MD simulations can give some qualitative guidelines for DFT calculations with remarkably smaller computing costs. The resultant deviations between the DFT calculations and MD simulations may attribute to the neglecting of vibrational energy and free energy in DFT calculations and the errors introduced by ReaxFF parameterization, which will be systematically studied in our future works.

Besides the critical strain for phase transition, the phase transition structure and fracture strain are also very important. After the initiation of phase transition, the phase transition region quickly spread as the loading proceeds before the fracture of MBP. Figure 5 gives the fracture configurations of SW-2 defective and pristine MBP under different loading paths. The phase transition region is marked by dashed lines in Figure 5(a) and 5(c). The relative positions of the initial phase transition strain in armchair direction is sketched in figure 5(b) according to the results in Figure 4. For SW-2 defective MBP under loading path A, O, G, the phase transition region spreads all over the sample before fracture. While, for the SW-2 defective MBP under loading path J, though its initial phase transition strain is small, its fracture strain is also small, so that only a part of the sample is phase transformed. For the pristine MBP, the similar trend is observed, but the phase transition region is much smaller than that of the SW-2 defective MBP. Besides, the phase transition region under loading path B is the smallest for both of the SW-2 defective and pristine MBP due to the maximum initial phase transition strain. Therefore, the gap between the fracture strain and initial phase transition strain is an important factor to influence the phase transition region in MBP. The SW-2 defect can be regarded as an excellent ‘phase transition catalyzer’ for MBP to

significantly decrease the initial phase transition strain and increase the homogeneity of phase transition.

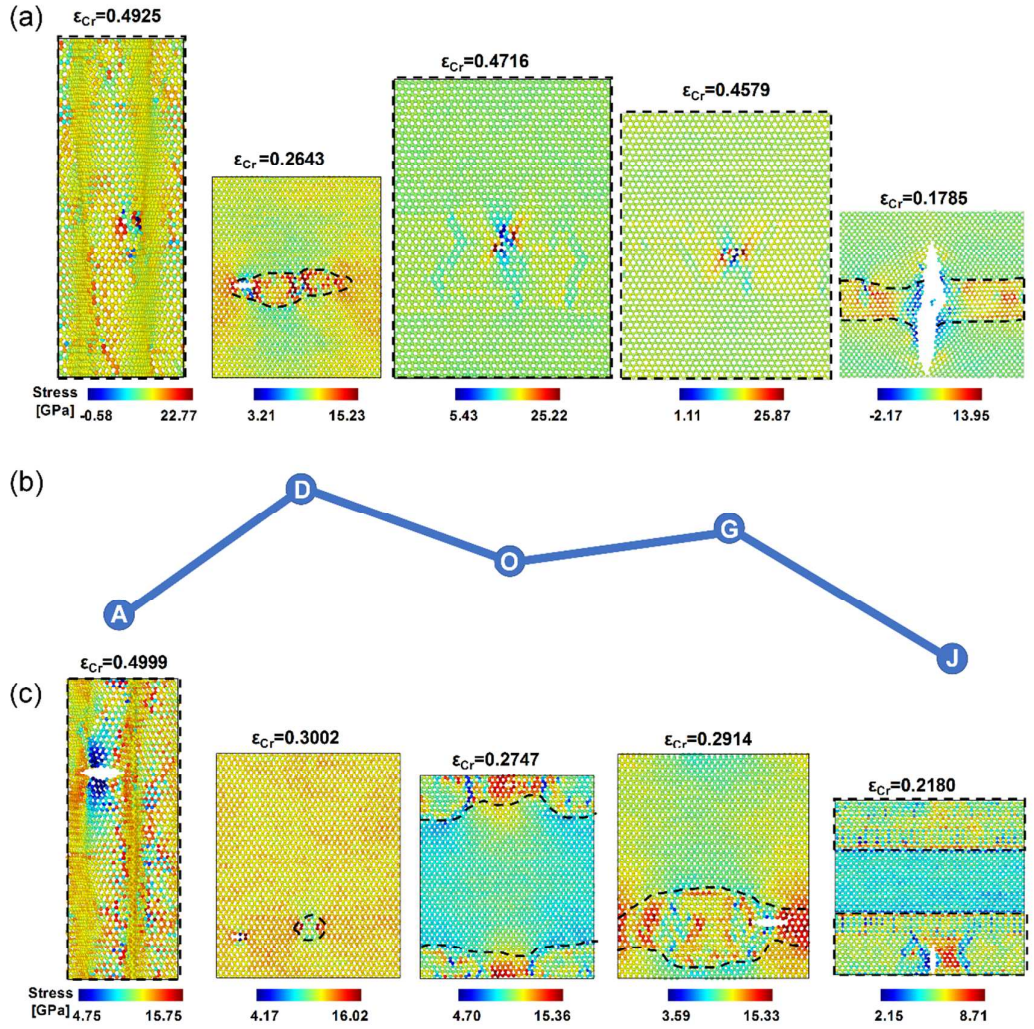

Figure 5. Phase transition structures and fracture modes under different loading paths. The fracture configurations and the corresponding normal stress in armchair direction are shown for SW-2 defective MBP (a) and pristine MBP (c). (b) The relative positions of the critical strain in armchair direction for phase transition under different loading paths corresponding to Figure 3 and Figure 4. The fracture strains for SW-2 defective and pristine MBP under different loading paths are listed at the top of each figure. The phase transition regions are marked by dashed lines.

3.3 Phase transition under staged loading

In this section, the phase transition of SW-2 defective and pristine MBP under staged loading is explored. The staged loading is achieved by first applying a pre-strain in zigzag direction,

and then a uniaxial tensile strain in armchair direction is applied with keeping the pre-strain in zigzag direction. Different loading paths for the staged loading mode are illustrated in Figure 6(a) and the corresponding pre-strain in zigzag direction is given in Figure 6(b). Compared with the proportional loading presented in Section 3.2, the staged loading can be treated as two individual uniaxial loadings, which may be easier to realize in experiments and have different effects on the phase transition of MBP from that of biaxial proportional loading. Here, the strain rate in both of the zigzag and armchair deformation is 5×10^{-8} fs^{-1} for all of the MD simulation cases in this section.

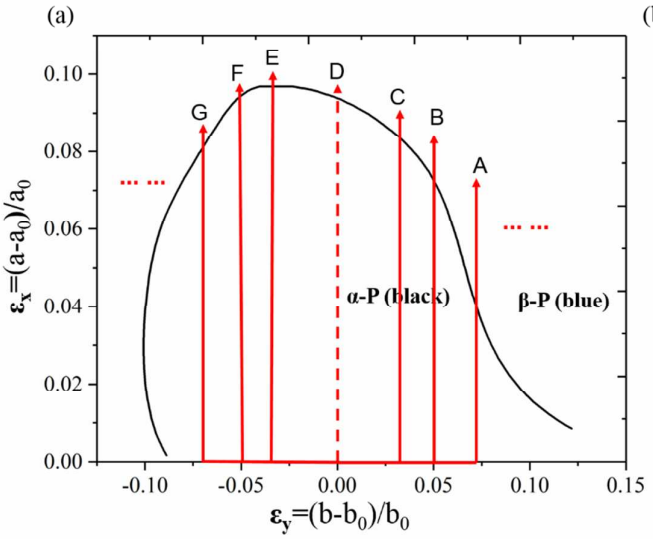

Strain rate: 5×10^{-8} fs^{-1}

Tension	Zigzag Strain
……	……
A	0.07
B	0.05
C	0.03
D	0
E	-0.03
F	-0.05
G	-0.07
……	……

Figure 6. The illustrations of the staged loading. (a) Different loading paths on the intersection contour of energy surfaces for SW-2 defective monolayer α-P and β-P under biaxial strain. (b) Pre-strain in zigzag direction corresponding to the loading path in (a). The strain rate in the deformation of zigzag and armchair direction is set as 5×10^{-8} fs^{-1} for all of the loading paths. The settings for pristine MBP is just the same.

Figure 7 illustrates the critical strain in armchair direction for the phase transition of pristine and SW-2 defective MBP under different loading paths in Figure 6(a). The red and black data points in Figure 7 indicate the occurrence of phase transition in SW-2 defective and pristine MBP. However, for SW-2 defective MBP, the self-healing of the SW-2 defect can be observed with zigzag pre-strain larger than 0.04 (exclude 0.04) in consistent with our

previous work , as indicated in Figure 7. While, for pristine MBP under the zigzag pre-strain ranging from 0 to -0.05 (exclude -0.05), no phase transition is observed before the fracture of MBP, as dot-dashed line in Figure 7. In general, the trend of the critical phase transition strain under staged loadings is similar with that of the proportional loading. The large pre-strain in zigzag direction can promote the phase transition. Besides, the critical phase transition strain of pristine MBP is also larger than that of SW-2 defective MBP.

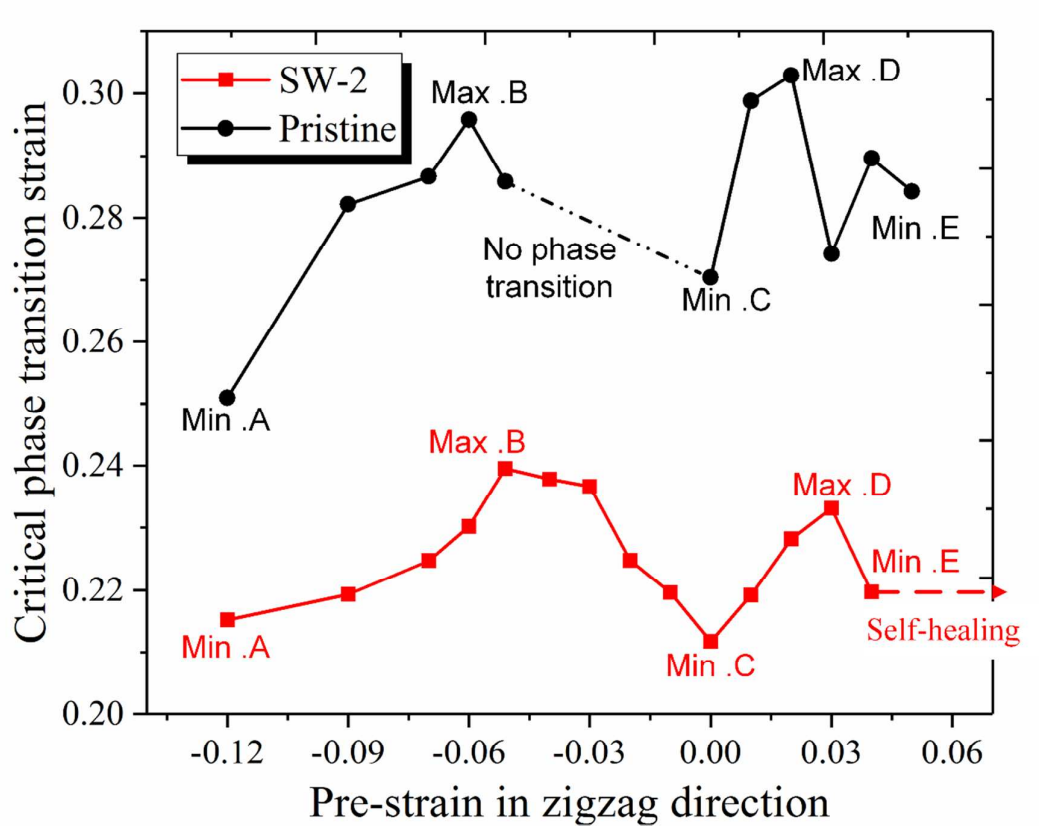

Figure 7. Critical strain in armchair direction for phase transition of SW-2 defective and pristine MBP versus different pre-strain in the zigzag direction. Self-healing is observed for SW-2 defective MBP with zigzag pre-strain larger than 0.04. For pristine MBP with zigzag pre-strain ranging from 0 to -0.04, no phase transition is observed. The marked symbols Min. A, Max. B, Min. C, Max. D and Min. E indicate the relative positions of the critical strain.

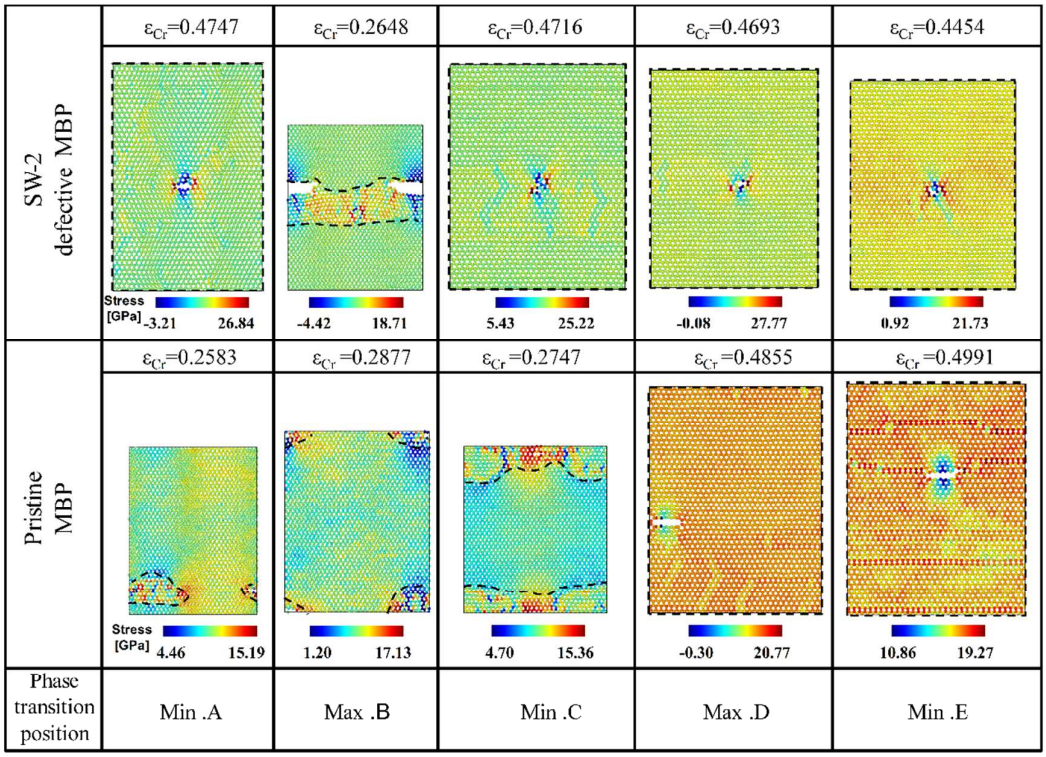

Figure 8. Phase transition structures and fracture modes under different staged loading paths. The fracture configurations and the corresponding normal stress in armchair direction are shown for SW-2 defective MBP and pristine MBP. The relative positions of the critical strain in armchair direction for phase transition are labeled as Min. A, Max. B, Min. C, Max. D, Min. E, corresponding to that in Figure 7. The fracture strains for SW-2 defective and pristine MBP are listed at the top of each figure. The phase transition regions are marked by dashed lines.

Figure 8 shows the fracture configurations and phase transition regions for the SW-2 defective and pristine MBP under different staged loading paths. For SW-2 defective MBP, the phase transition region spreads all over the sample before the fracture of MBP, expect for the staged loading path B due to the small gap between the fracture strain and critical phase transition strain. For pristine MBP, under small tensile pre-strain in zigzag direction, the phase transition region can also spread all over the sample for stage loading paths D and E, as shown in Figure 8. While under small compressive pre-strain or fixed in zigzag direction, only a part of the pristine MBP is phase transformed, as the loading path A, B and C in Figure 8. Indeed, the size of the phase transition region is significantly influenced by the gap

between the fracture strain and critical phase transition strain of MBP. The staged loading mode is beneficial to increase the fracture strain for most of the simulation cases so as to get higher homogeneity of the phase transition.

3.4 Effect of SW-2 defect concentration

In this section, the effect of SW-2 defect concentration on phase transition of MBP is studied. Without loss of generality, we construct different number of SW-2 defect (i.e. 1, 4, 9, 16, 25, 36 SW-2 defects) in the MBP sheet with dimensions about 10 nm × 10 nm. The SW-2 defects are uniformly distributed in the MBP sheet, as shown in Figure 10. Random distribution of SW-2 defect is also considered. Other complex distributions of the SW-2 defects will be discussed in the future.

Figure 9 gives the stress-strain curves of MBP with different SW-2 defect concentrations under uniaxial tension in armchair direction. The strain rate is 1.0×10^{-8} fs^{-1}. For both uniformly and randomly distributed SW-2 defect, the stress-strain curves are almost overlapped before the initiation of phase transition. Therefore, the influence of SW-2 defect concentration on the Young's modulus of MBP is negligible as the effect of SW-2 defect is "local".[40] But as discussed before, SW-2 defect can be a good 'phase transition catalyzer' to promote the phase transition of MBP. Thus, the critical phase transition strain is smaller for higher concentration of SW-2 defect in uniform distribution, which can be observed from the marked region in Figure 9(a). While for randomly distributed SW-2 defects, no phase transition can be observed before final failure of MBP when the number of SW-2 defect is larger (i.e., 25 SW-2 defects per 100 nm^2 in this study), as shown in Figure 9(b). As the SW-2 defect causes stress concentration in MBP and the concentration of SW-2 defect may generate large stress concentration, the competition of fracture and phase transition determine the mechanical behaviors of MBP. If the number of SW-2 defects is small, the critical phase transition strain is smaller for higher concentration of SW-2 defect too, which can be observed from the marked region in Figure 9(b), just as that for uniformly distributed situation. Thus, the proper concentration of SW-2 defect with uniform distribution is beneficial for the phase transition of MBP.

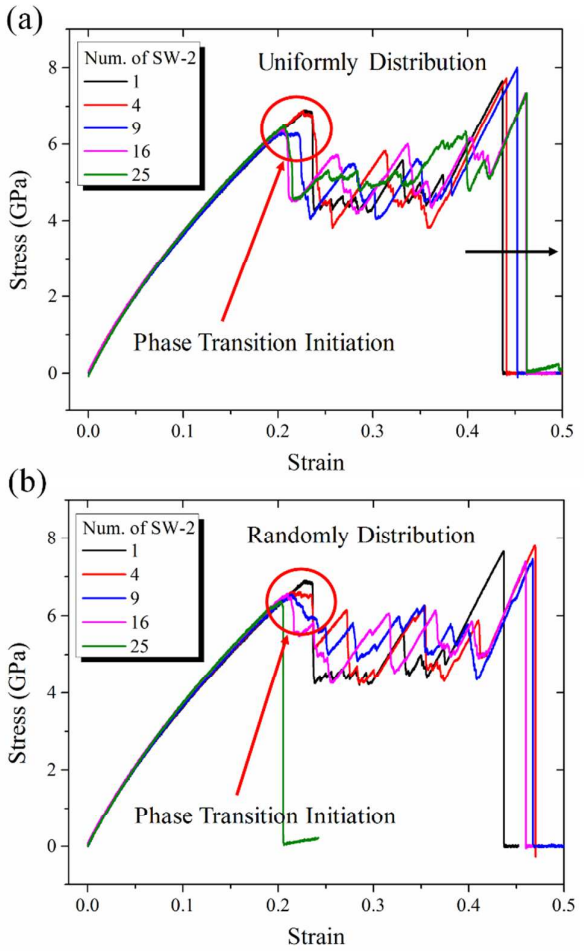

Figure 9. Tensile stress-strain curves of MBP with different SW-2 defect concentrations under uniaxial tension in armchair direction. (a) Uniform distribution (b) random distribution. The marked region corresponds to the initiation of phase transition.

Besides, the SW-2 defect concentration can also influence the fracture strain of MBP so as to influence the spreading and homogeneity of the phase transition. Take uniformly distributed SW-2 defects as an example, Figure 10 illustrates the fracture configuration and stress distribution of MBP with different SW-2 concentrations under uniaxial tension in armchair direction. It is observed that the phase transition region spreads over all of the sample for the number of SW-2 defect ranging from 1 to 36. Besides, the fracture strain increases with the increasing of SW-2 defect concentration, as shown in Figure 10. This can be explained by the compositions of the phase transition. As the phase transition around SW-2 defect is dominated by β-P, the higher SW-2 defect concentration in MBP correspond to higher ratio of β-P to γ-P in the phase transition region. While, the lattice constant of β-P is

larger than that of γ-P in armchair direction, i.e. 5.77 Å versus 5.34 Å,[18] and the higher composition of β-P can sustain larger fracture strain. Therefore, we can conclude that the SW-2 defect is beneficial for the phase transition initiation and spreading, which provides an effective strain engineering routine for tuning the structures of MBP. Note that the nonuniform distribution of SW-2 defect also make the fracture behaviors of MBP become elusive, and further efforts remain to be carried out for studying the effect of distribution.

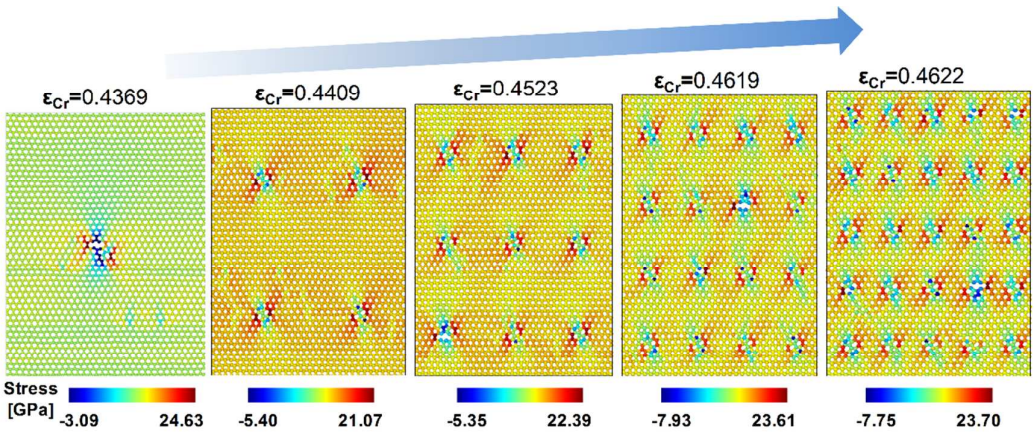

Figure 10. The fracture configurations and stress distributions of MBP with different number of uniformly distributed SW-2 defect under uniaxial tension in armchair. The corresponding fracture strain ε_{Cr} is given on the top of each figure. The color contour represents the normal stress in armchair direction.

3.5 Effect of MBP curvature

The initial curvature of a thin elastic membrane could stimulate or suppress the initiation of fracture, tune the paths of cracks propagation, and also control the behaviors of pleats and defects.[54-56] Due to the small bending stiffness of MBP, they are very easy to buckle to curved configurations under compressive or shear loadings.[57, 58] Therefore, to clarify the curvature effect on the phase transition of MBP is also an important issue. In this section, we construct a series of MBP nanotube (α-PNT) with different radii (i.e. different curvatures) to study the curvature effect on phase transition of MBP. The uniaxial tension is applied in the axial direction of α-PNT (armchair direction). The phase transition from α-P to a mixture of β-P and γ-P can always be observed for both of the SW-2 defective and pristine α-PNT. Figure 11 illustrates the fracture configurations and stress distributions of α-PNT with different radii. It is shown that for SW-2 defective α-PNT, its fracture strain increases with the increasing of

tube radius, and the phase transition region spreads all over the α-PNT before fracture, as shown in Figure 11(a). While, for the pristine α-PNT, its fracture strain increases with the increasing of tube radius for small radius α-PNT (i.e. chirality (n, 0), n≤45), where the phase transition region spreads all over the tube. For pristine α-PNT with large radius (n>45), only a part of the tube is phase transformed and the fracture strain is significantly reduced, as shown in Figure 11(b). Note that for α-PNT with smaller radius (n<20), the tube structure will collapse to a closed-edged bilayer phosphorene during axial tension.[59]

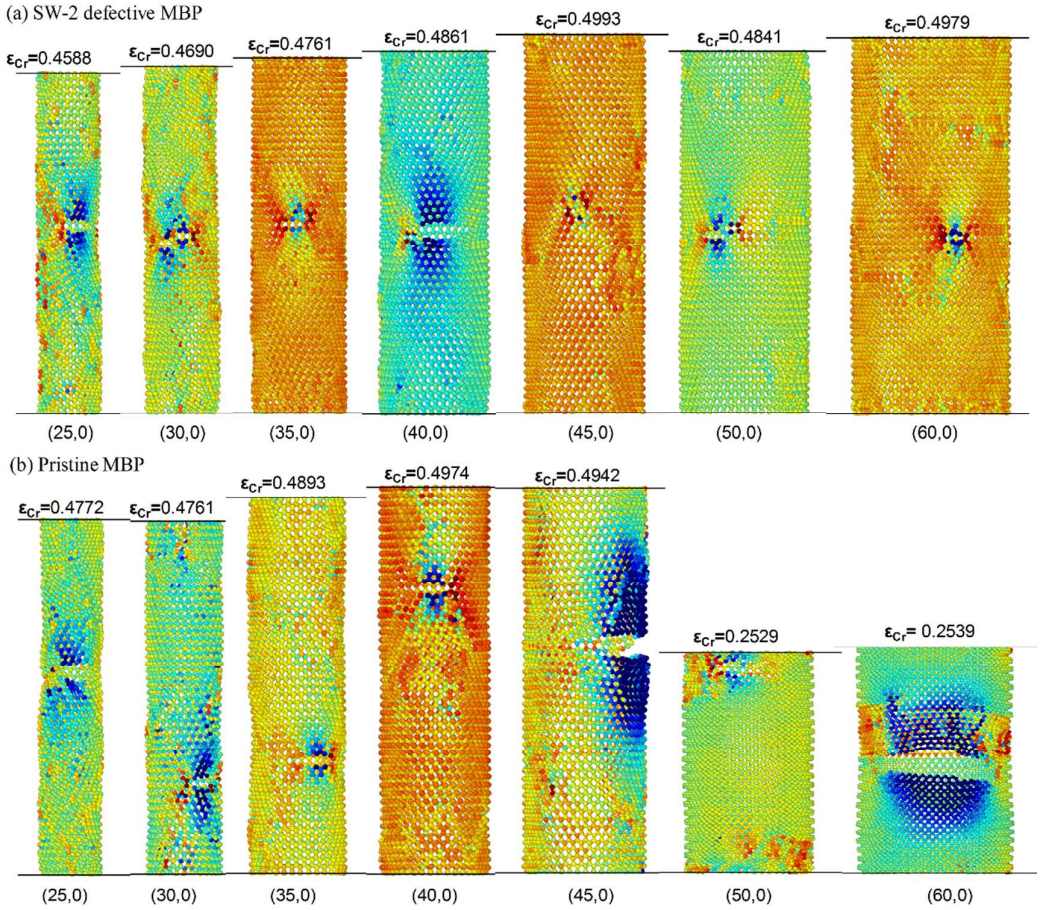

Figure 11. Fracture configurations and stress distributions of SW-2 defective (a) and pristine (b) α-PNT with different radii. The chirality and fracture strain of the α-PNT are marked on the bottom and top of each figure, respectively. Color contour represents the normal stress distribution in the axial direction.

Figure 12 shows the critical phase transition strain of SW-2 defective and pristine α-PNT with different radii. It is shown that the critical phase transition strain linearly decreases with the increasing of curvature, i.e. the decreasing of α-PNT radius. This may partly explain the

large compressive strain can promote the phase transition of MBP in Section 3.2 and 3.3, as the compressive strain may cause buckling deformation of MBP to generated curved configuration. Besides, SW-2 defects can also promote the phase transition of α-PNT (i.e. smaller critical phase transition strain compared to that of pristine α-PNT) and the critical phase transition strain for SW-2 defective α-PNT is also more sensitive to the curvature than that of the pristine α-PNT (i.e. the slope of the critical strain-curvature curve of the SW-2 defective α-PNT (-0.2070) is about two times of the pristine α-PNT (-0.1066)), as shown in Figure 12. Indeed, temperature is another important factor for the phase transition of α-PNT. A comparable MD simulation at 1.0 K for pristine and SW-2 defective PNT has also been conducted, and the phase transition cannot be observed, in consistent with the previous results obtained from density functional tight-binding calculations at 0 K.[60] The system with higher temperature has larger actuation energy, which is more helpful to overcome the energy barrier of phase transition. In this work we focus on the phase transition of MBP in the view of potential energy of different phases based on DFT calculations and dynamic phase transition process based on MD simulations. The energy barrier of the phase transition as well as temperature effect on phase transition be explored in our future works.

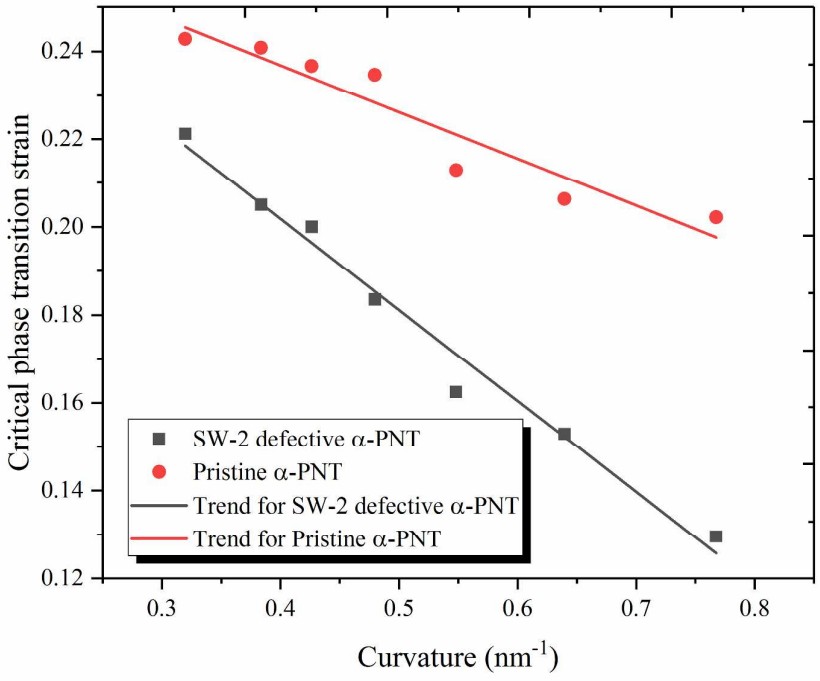

Figure 12. Critical phase transition strain versus curvature for pristine and SW-2 defective α-PNT. The symbols are obtained from MD simulations and the solid lines are linear fitting.

4. Outlook and conclusions

In this work, the phase transition of MBP to a mixed phase of β-P and γ-P is systematically explored by combining DFT calculations and MD simulations using ReaxFF. It is found that SW-2 defect in MBP can serve as an excellent 'phase transition catalyzer', significantly decreasing the critical strain for phase transition and increasing the homogeneity of phase transition. In general, the phase transition of MBP is primarily driven by the tension strain in armchair direction, and the large tensile or compressive strain in zigzag direction can promote the phase transition, while a small compressive strain in zigzag direction prevents the phase transition. For most of the simulation cases, the MBP has larger fracture strain under staged loading than that of proportional loading, so that the phase transition structure under staged loading is more uniform. Moreover, the phase transition of MBP is also influenced by SW-2 defect concentration and curvature, and the critical phase transition strain decreases with the increasing of SW-2 defect concentration and curvature. Overall, the results presented herein provide useful insights for tuning the atomic structures of monolayer phosphorus allotropes by strain and defect engineering, which may hold potential applications in electronic, thermal and optical devices.

Conflicts of interest

There are no conflicts of interest to declare.

Acknowledgment

Y.L. acknowledges the support from the National Natural Science Foundation of China (No. 11572239) and National Key Research and Development Program of China (No. 2016YFB0700300). X.C. acknowledges the support from the National Natural Science Foundation of China (Nos. 11372241 and 11572238), ARPA-E (DE-AR0000396) and AFOSR (FA9550-12-1-0159).

References

1. E. S. Reich, *Nature*, 2014, **506**, 19.
2. L. Li, Y. Yu, G. J. Ye, Q. Ge, X. Ou, H. Wu, D. Feng, X. H. Chen and Y. Zhang, *Nat Nanotechnol*, 2014, **9**, 372-377.
3. M. Pumera, *Angew Chem Int Ed Engl*, 2017, **56**.
4. K. Watanabe, T. Taniguchi and H. Kanda, *Nat Mater*, 2004, **3**, 404-409.
5. M. Chhowalla, H. S. Shin, G. Eda, L. J. Li, K. P. Loh and H. Zhang, *Nature Chemistry*, 2013, **5**, 263-275.
6. M. KF, L. C, H. J, S. J and H. TF, *Physical review letters*, 2010, **105**, 136805.
7. N. KS, J. D, S. F, B. TJ, K. VV, M. SV and G. AK, *Proceedings of the National Academy of Sciences of the United States of America*, 2005, **102**, 10451.
8. L. Tao, E. Cinquanta, D. Chiappe, C. Grazianetti, M. Fanciulli, M. Dubey, A. Molle and D. Akinwande, *Nature Nanotechnology*, 2015, **10**, 227-231.
9. Q. X, L. J, F. L and L. J, *Science (New York, N.Y.)*, 2014, **346**, 1344-1347.
10. K. S. Novoselov, A. K. Geim, S. V. Morozov, D. Jiang, Y. Zhang, S. V. Dubonos, I. V. Grigorieva and A. A. Firsov, *Science*, 2004, **306**, 666-669.
11. J. Qiao, X. Kong, Z. X. Hu, F. Yang and W. Ji, *Nat Commun*, 2014, **5**, 4475.
12. X. Han, H. M. Stewart, S. A. Shevlin, C. R. Catlow and Z. X. Guo, *Nano Letters*, 2014, **14**, 4607.
13. H. Liu, A. T. Neal, Z. Zhu, Z. Luo, X. Xu, D. Tomanek and P. D. Ye, *ACS Nano*, 2014, **8**, 4033-4041.
14. J. P. Xu, J. Q. Zhang, H. Tian, H. Xu, W. K. Ho and M. H. Xie, *Phys Rev Mater*, 2017, **1**.
15. J. L. Zhang, S. Zhao, C. Han, Z. Wang, S. Zhong, S. Sun, R. Guo, X. Zhou, C. D. Gu, K. D. Yuan, Z. Li and W. Chen, *Nano Lett*, 2016, **16**, 4903-4908.
16. M. Wu, H. Fu, L. Zhou, K. Yao and X. C. Zeng, *Nano Lett*, 2015, **15**, 3557-3562.
17. Z. Zhu and D. Tomanek, *Phys Rev Lett*, 2014, **112**, 176802.
18. J. Guan, Z. Zhu and D. Tomanek, *Phys Rev Lett*, 2014, **113**, 046804.
19. J. W. Jiang and H. S. Park, *Nat Commun*, 2014, **5**, 4727.
20. R. Fei and L. Yang, *Nano Lett*, 2014, **14**, 2884-2889.
21. M. Z. Rahman, C. W. Kwong, K. Davey and S. Z. Qiao, *Energ Environ Sci*, 2016, **9**, 709-728.
22. B. Ghosh, S. Nahas, S. Bhowmick and A. Agarwal, *Phys Rev B*, 2015, **91**, 115433.
23. Y. Li and X. Chen, *2D Materials*, 2014, **1**, 031002.
24. D. Akinwande, C. J. Brennan, J. S. Bunch, P. Egberts, J. R. Felts, H. Gao, R. Huang, J. S. Kim, T. Li and Y. Li, *Extreme Mechanics Letters*, 2017, **13**.
25. K. N. Duerloo and E. J. Reed, *Acs Nano*, 2015, **10**, 289.
26. Y. Zhou and E. J. Reed, *J Phys Chem C*, 2015, **119**, 21674-21680.
27. Y. Li, K. A. Duerloo, K. Wauson and E. J. Reed, *Nat Commun*, 2016, **7**, 10671.
28. J. Deng, Z. Chang, T. Zhao, X. Ding, J. Sun and J. Z. Liu, *J Am Chem Soc*, 2016, **138**, 4772-4778.
29. K. A. Duerloo, Y. Li and E. J. Reed, *Nat Commun*, 2014, **5**, 4214.
30. Y. Wang, J. Xiao, H. Zhu, Y. Li, Y. Alsaid, K. Y. Fong, Y. Zhou, S. Wang, W. Shi, Y. Wang, A. Zettl, E. J. Reed and X. Zhang, *Nature*, 2017, **550**, 487-491.
31. M. Kan, J. Y. Wang, X. W. Li, S. H. Zhang, Y. W. Li, Y. Kawazoe, Q. Sun and P. Jena, *J Phys Chem C*, 2015, **118**, 1515–1522.
32. B. S. Sa, Y. L. Li, J. S. Qi, R. Ahuja and Z. M. Sun, *J Phys Chem C*, 2014, **118**, 26560-26568.
33. L. Kou, A. Du, C. Chen and T. Frauenheim, *Nanoscale*, 2014, **6**, 5156-5161.
34. A. Jain and A. J. McGaughey, *Sci Rep*, 2015, **5**, 8501.

35. Z. Y. Ong, Y. Q. Cai, G. Zhang and Y. W. Zhang, *J Phys Chem C*, 2014, **118**, 25272-25277.
36. M. N. Blonsky, H. L. Zhuang, A. K. Singh and R. G. Hennig, *ACS nano*, 2015, **9**, 9885-9891.
37. W. Wu, L. Wang, R. Yu, Y. Liu, S. H. Wei, J. Hone and Z. L. Wang, *Advanced Materials*, 2016, **28**, 8463-8468.
38. S. E. Boulfelfel, G. Seifert, Y. Grin and S. Leoni, *Phys.rev.b*, 2012, **85**, 64-68.
39. J. C. Jamieson, *Science*, 1963, **139**, 1291.
40. Y. Chen, H. Xiao, Y. Liu and X. Chen, *J Phys Chem C*, 2018, **122**, 6368-6378.
41. W. Hu and J. L. Yang, *J Phys Chem C*, 2015, **119**, 20474-20480.
42. P. Giannozzi, S. Baroni, N. Bonini, M. Calandra, R. Car, C. Cavazzoni, D. Ceresoli, G. L. Chiarotti, M. Cococcioni, I. Dabo, A. Dal Corso, S. de Gironcoli, S. Fabris, G. Fratesi, R. Gebauer, U. Gerstmann, C. Gougoussis, A. Kokalj, M. Lazzeri, L. Martin-Samos, N. Marzari, F. Mauri, R. Mazzarello, S. Paolini, A. Pasquarello, L. Paulatto, C. Sbraccia, S. Scandolo, G. Sclauzero, A. P. Seitsonen, A. Smogunov, P. Umari and R. M. Wentzcovitch, *J Phys Condens Matter*, 2009, **21**, 395502.
43. P. JP, B. K and E. M, *Physical Review Letters*, 1996, **77**, 3865.
44. H. J. Monkhorst and J. D. Pack, *Phys Rev B*, 1976, **13**, 5188.
45. X. H. Peng, Q. Wei and A. Copple, *Phys Rev B*, 2014, **90**, 085402.
46. J. Xiao, M. Long, C. S. Deng, J. He, L. L. Cui and H. Xu, *J Phys Chem C*, 2016, **120**.
47. S. Plimpton, *J Comput Phys*, 1995, **117**, 1-19.
48. H. Xiao, X. Shi, F. Hao, X. Liao, Y. Zhang and X. Chen, *J Phys Chem A*, 2017, **121**, 6135-6149.
49. J. W. Jiang, *Nanotechnology*, 2015, **26**, 315706.
50. H. J. Conley, B. Wang, J. I. Ziegler, H. R. Jr, S. T. Pantelides and K. I. Bolotin, *Nano Letters*, 2013, **13**, 3626-3630.
51. S. P. Koenig, N. G. Boddeti, M. L. Dunn and J. S. Bunch, *Nature Nanotechnology*, 2011, **6**, 543-546.
52. Z. Wang, J. Lee, K. He, J. Shan and P. X. L. Feng, *Scientific Reports*, 2014, **4**, 3919.
53. D. Lloyd, X. Liu, J. W. Christopher, L. Cantley, A. Wadehra, B. L. Kim, B. B. Goldberg, A. K. Swan and J. S. Bunch, *Nano Letters*, 2016, **16**.
54. W. T. Irvine, V. Vitelli and P. M. Chaikin, *Nature*, 2010, **468**, 947.
55. N. P. Mitchell, V. Koning, V. Vitelli and W. T. M. Irvine, *Nature Materials*, 2017, **16**, 89.
56. V. Vitelli, J. Lucks and D. Nelson, *Proceedings of the National Academy of Sciences of the United States of America*, 2006, **103**, 12323-12328.
57. P. Cao, J. Wu, Z. Zhang and F. Ning, *Nanotechnology*, 2016, **28**, 045702.
58. G. Wang, G. C. Loh, R. Pandey and S. P. Karna, *Nanotechnology*, 2015, **27**, 055701.
59. X. Liao, H. Xiao, X. Lu, Y. Chen, X. Shi and X. Chen, *Nanotechnology*, 2018, **29**, 085707.
60. V. Sorkin and Y. W. Zhang, *Nanotechnology*, 2016, **27**, 395701.

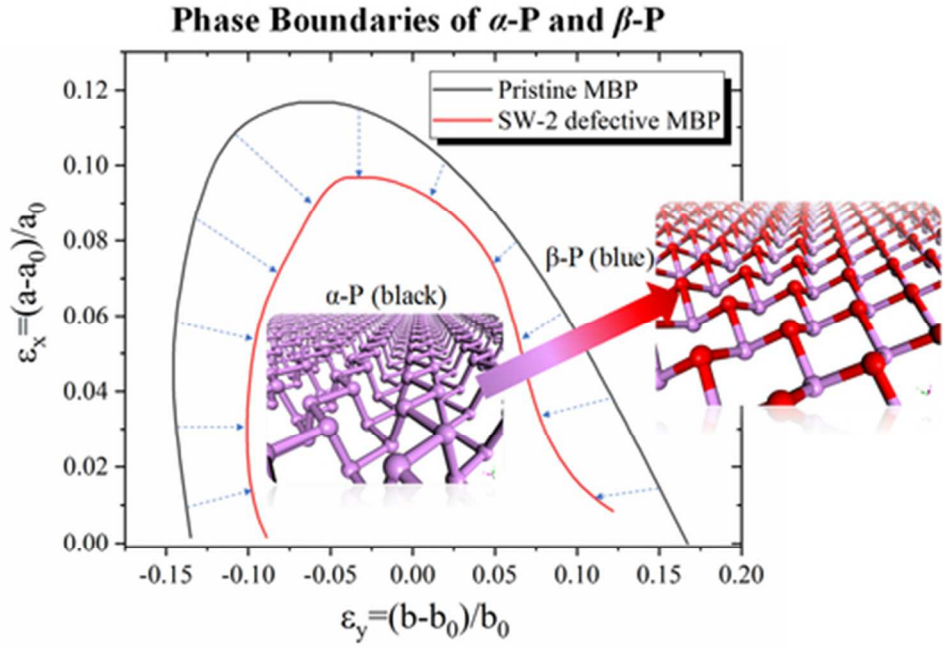

39x28mm (300 x 300 DPI)